Int J Adv Manuf Technol (2010) 48:671–689
DOI 10.1007/s00170-009-2294-2

ORIGINAL ARTICLE

Automatic surface inspection for directional textures using nonnegative matrix factorization

Der-Baau Perng · Ssu-Han Chen

Received: 27 March 2009 / Accepted: 2 September 2009 / Published online: 17 September 2009
© Springer-Verlag London Limited 2009

Abstract A global image restoration scheme using nonnegative matrix factorization (NMF) is proposed in this paper. This NMF-based image restoration scheme can be used for inspecting the defects in directional texture surfaces automatically. Decomposing the gray level of image pixels into an ensemble of row vectors, we first reduce the data set from original data space into a lower-dimensional NMF space. The repetitive and periodical primitives are well reconstructed by two lower-dimensional basis and weight matrices with nonnegative elements, named nonnegative matrix approximation (NMA). Then the local defects will be revealed by applying image subtraction between the original image and the NMA. As a consequence, the directional textures are eliminated, and only local defects are preserved if they initially are embedded in the surface. A supervised heuristic, elbow of residual curve rule, is devised which helps users to determine a proper basis space size of a specific image. Experiments on a variety of directional texture surfaces are given to demonstrate the effectiveness and robustness of the proposed method.

Keyword Directional texture · Nonnegative matrix factorization · Defect inspection · Machine vision

D.-B. Perng (✉) · S.-H. Chen
Department of Industrial Engineering and Management,
National Chiao Tung University,
Hsinchu, Taiwan 30010
e-mail: perng@cc.nctu.edu.tw

1 Introduction

Directional texture is a set of line primitives in some regular or repetitive arrangement over an entire texture region. Directional texture has a homogeneous configuration and is commonly found on machined parts, semiconductor products, nature woods, and fabric textiles. Detecting local defects embedded in a directional texture surface is a common application of computer vision. Numerous approaches to the problem have been proposed, including statistical, structural, spatial domain filtering, spectral domain filtering, and model-based approaches [1, 2]. The methods which are less affected by noise and are immune to the limitations of local feature extraction or template matching are always recommended such as the Fourier transform [3, 4], the wavelet transform [5], the Gabor filter [6, 7], the golden-block-based self-refining algorithm [8], the singular-value decomposition [9], the anisotropic kernel [10], the independent component analysis [11], and the principal component analysis [12]. These are widely used in surface quality control.

This paper proposes a new defect inspector for directional textures based on the nonnegative matrix factorization (NMF). NMF factors a matrix **X** into two submatrices, **W** and **H**, where **W** has far fewer columns than **X**, and **H** has far fewer rows than **X**. A nonnegative matrix approximation (NMA) can be generated to determine the latent structure in the data. In general, negative elements of the factored matrix will contradict the physical realities in many applications. The pixels in a grayscale image are one example; they must have nonnegative intensities—otherwise, they cannot be interpreted rationally. To tackle this philosophical dilemma, NMF enforces the constraint that the elements of the two submatrices must be nonnegative such that this factoring technique can be used more readily

with digital image processing. For a directional texture surface, the two decomposed lower-dimensional submatrices involve the texture basis; they are ideally suited for characterizing the repetitive and periodic line primitives in grayscale images. Local defects are preserved by image subtraction of the original image from the reconstructed NMA.

Underspecification or overspecification of the basis space size, however, distorts the results. The obvious problem of underspecification involves the loss of texture information in the NMA. The effects of overspecification may incorrectly result in including the defects in the NMA. This paper describes a supervised heuristic elbow of residual curve (ERC) rule that is developed to enable users to extract the proper basis space size automatically. Some preliminary experiments are discussed to demonstrate that the proposed NMF-based image restoration scheme with the ERC rule is effective and robust when used for inspecting various defects on distinct directional texture surfaces.

The rest of this paper is organized as follows. In Section 2, we review the NMF applications to computer vision. In Section 3, we describe the proposed NMF-based image restoration scheme. In Section 4, we present the experimentation and corresponding results. Our concluding remarks are discussed in Section 5.

2 NMF applications to computer vision

NMF comes from studies of positive matrix factorization (PMF) in the middle 1990s [13]. The goal was to use factor

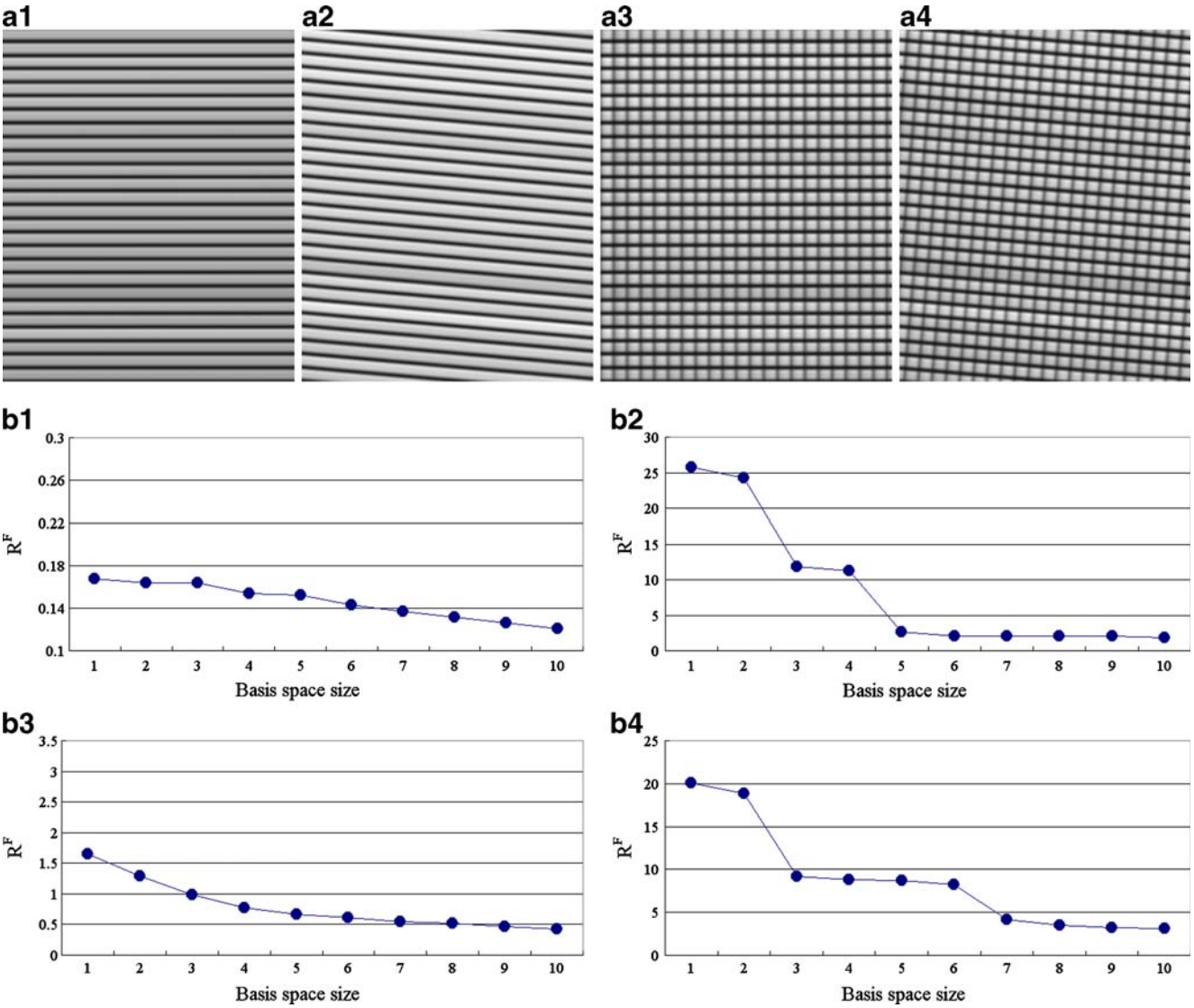

Fig. 1 (*a1–a4*) Four artificial images with different linear primitives; and (*b1–b4*) the corresponding residual curves

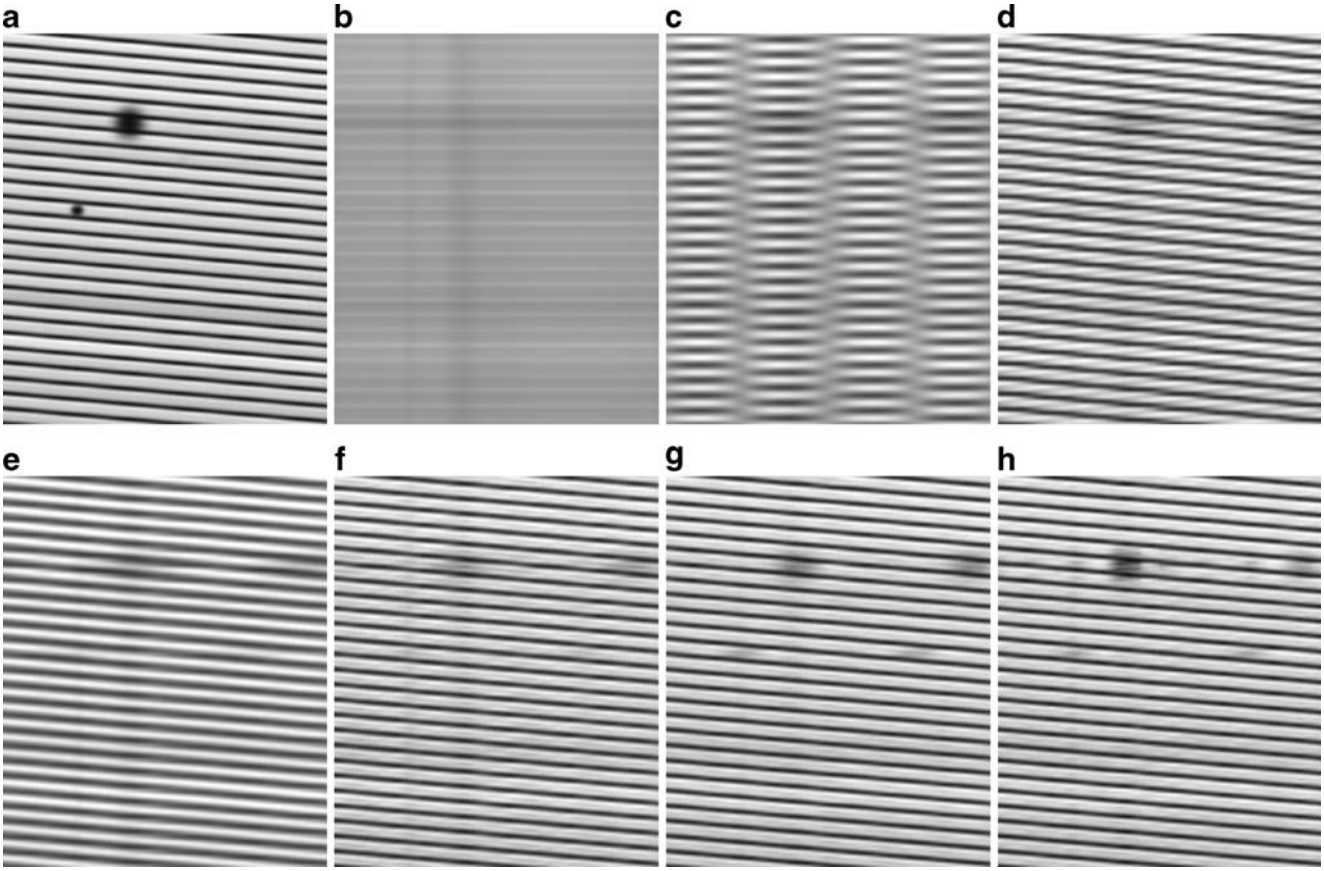

Fig. 2 **a** Artificial spot defective image; and **b**–**h** NMAs with k=1, 2,..., 7, respectively

analysis on environmental data to find a small number of root causes that explained a large set of measurements. PMF then became more widely known as NMF after the seminal paper of Lee and Seung [14] that demonstrated how to obtain a parts-based representation for facial image data. Many researchers subsequently used NMF to map samples into a low-dimensional and most-expressive feature space in the application of facial representation and recognition [15–17]. Other NMF applications in computer vision exist as well. Guillamet et al. introduced NMF to the context of image patch classification and recognition [18]. Liu and Zheng used NMF for object recognition [19]. Zhang et al. presented an image fusion method based on NMF [20]. In the field of real-time medical image analysis, Lee et al. showed that NMF would be feasible for image segmentation and factor extraction from dynamic image sequences in nuclear medicine [21]. Ahn et al. extended NMF to a multilayer network model for dynamic myocardial positron emission tomography image analysis [22]. Lee et al. used NMF to select discriminative features in the time–frequency representation of motor imagery electroencephalograms [23].

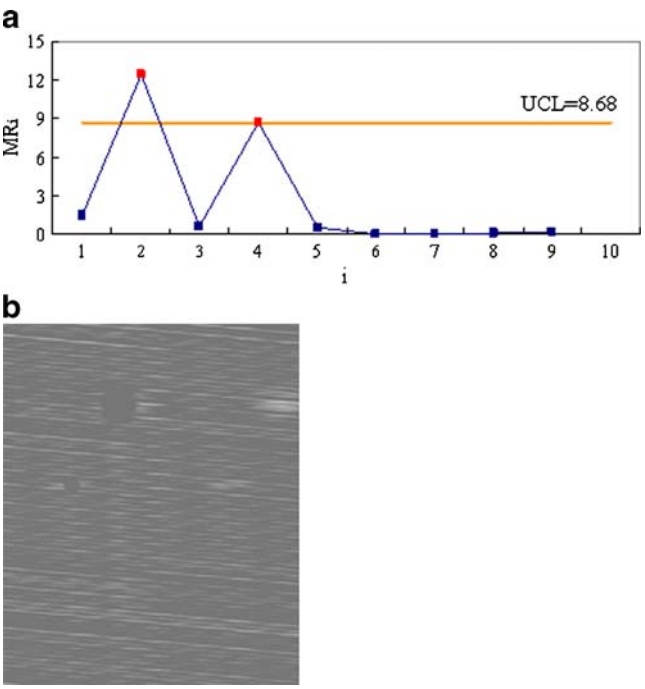

Fig. 3 **a** Moving range control chart of Fig. 1 (b2) in the training stage; and **b** restored image of Fig. 2a in the inspection stage

3 NMF-based defect detection

3.1 Nonnegative matrix factorization

We first slice image $\mathbf{X}$ of size $m \times n$ into an ensemble of m row vectors, $\mathbf{X}=[\mathbf{x}_1, \boldsymbol{x}_2, \ldots, \mathbf{x}_m]^{\mathrm{T}}$, and prespecify a positive integer $k < \min(m, n)$. NMF factors matrix $\mathbf{X}$ into two nonnegative submatrices, $\mathbf{W}$ of size $m \times k$ and $\mathbf{H}$ of size $k \times n$,

$$\mathbf{X} \approx \mathbf{WH} \tag{1}$$

where k is the basis space size that represents the intrinsic data dimensionality. Columns of $\mathbf{W}$ are the underlying basis vector, i.e., each of the n columns of $\mathbf{X}$ can be determined from k columns of $\mathbf{W}$. The columns of $\mathbf{H}$ contribute the weights associated with each basis vector. The fact that both $\mathbf{W}$ and $\mathbf{H}$ must be nonnegative is a natural requirement for image analysis.

The conventional approach to finding $\mathbf{W}$ and $\mathbf{H}$ has been to minimize the difference between $\mathbf{X}$ and $\mathbf{WH}$,

$$\begin{aligned} &\min_{W,\mathbf{H}} \mathrm{f}(\mathbf{W},\mathbf{H}) = \tfrac{1}{2}\|\mathbf{X}-\mathbf{WH}\|_{\mathrm{F}}^2 \\ &\text{s.t.} w_{ia} \geq 0, h_{bj} \geq 0, \forall i,a,b,j \end{aligned} \tag{2}$$

where $\|\cdot\|\mathrm{F}$ is the Frobenius or Hilbert-Schmidt norm. There are several algorithms for solving the bound-constrained optimization problem of Eq. 2, including the multiplicative update method [24] and the alternating nonnegative least squares with projected gradient (ANLSPG) method [25]. With faster convergence and strong optimization properties from the empirical experiments in [25], the ANLSPG algorithm is attractive for NMF learning and is used in this paper. The NMF k-dimensional decomposition with the ANLSPG learning algorithm is represented as a function of $\mathrm{NMF}_k(\mathbf{X})$ in the following sections.

The four artificial images containing well-defined periodic line structures either in unidirectional or in orthogonal form and with or without rotation shown in Fig. 1 (a1–a4) were used to demonstrate the approximation ability of NMF. We applied NMF to these images using basis space sizes of $\mathbf{W}$ and $\mathbf{H}$ from 1 to 10 and then calculated the corresponding Frobenius norm of the residuals between the original image and the reconstructed NMA simplified as a residual in the following sections. The residual curves resulting from Fig. 1 (a1–a4) for increasing basis space size are shown in the corresponding Fig. 1 (b1–b4). Note that the contours of Fig. 1 (b1–b4) decrease monotonically as the basis space size increased. In other words, the four NMAs were reasonably reconstructed closer and closer to the corresponding original images as the basis space size is larger and larger.

We also demonstrated the effect of basis space size on the approximation ability of NMF for faulty texture surfaces. Figure 2a is the same as Fig. 1 (a2) with artificial spot defects on it. We transformed Fig. 2a into NMF space and then reconstructed the NMAs using various basis space sizes. Figure 2b shows the NMA obtained by reconstructing the two nonnegative submatrices $\mathbf{W}$ and $\mathbf{H}$ with sizes of $m \times 1$ and $1 \times n$, respectively. Figure 2b is a uniformly reconstructed result where the background texture of Fig. 2a was not shaped at all. For k=2, the rotated line primitives of Fig. 2a were not well shaped, and only horizontal linear textures appeared, as shown in Fig. 2c. For k=3, the background texture of Fig. 2a was approximated as shown in Fig. 2d but accompanied by some blurring. The phenomena shown in Fig. 2b–d are the result of underspecification of k and involve a loss of texture information in NMA. For k=4 or k=5, the background texture of Fig. 2a was approximated relatively well, as shown in Fig. 2d, e, even if a few defects and some noise were present. These relatively structured results signify the directional texture of Fig. 2a, which was sufficiently represented for k=4 or k=5. For even larger values of k, the background texture was polluted with increasingly significant spot defects, as shown in Fig. 2f, g. These phenomena are the result of overspecification of k; defects in the NMA were wrongly included.

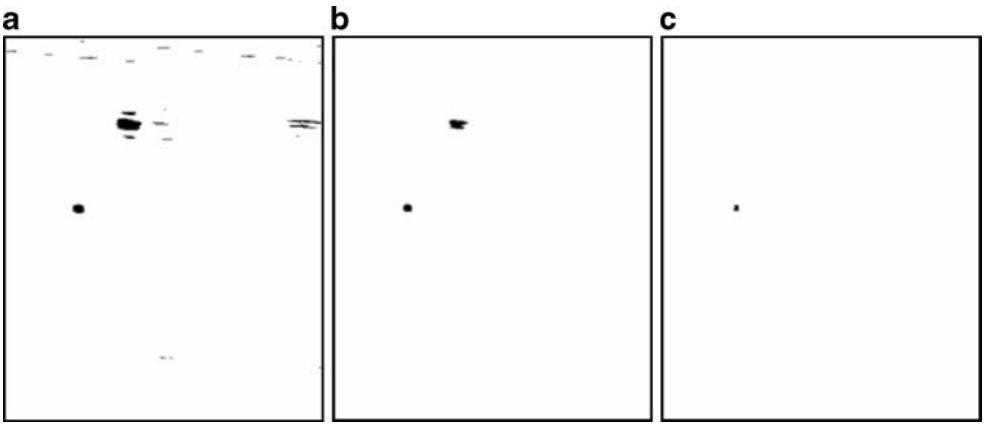

Fig. 4 Binarized image of Fig. 3b with **a** c=3, **b** c=5, and **c** c=7

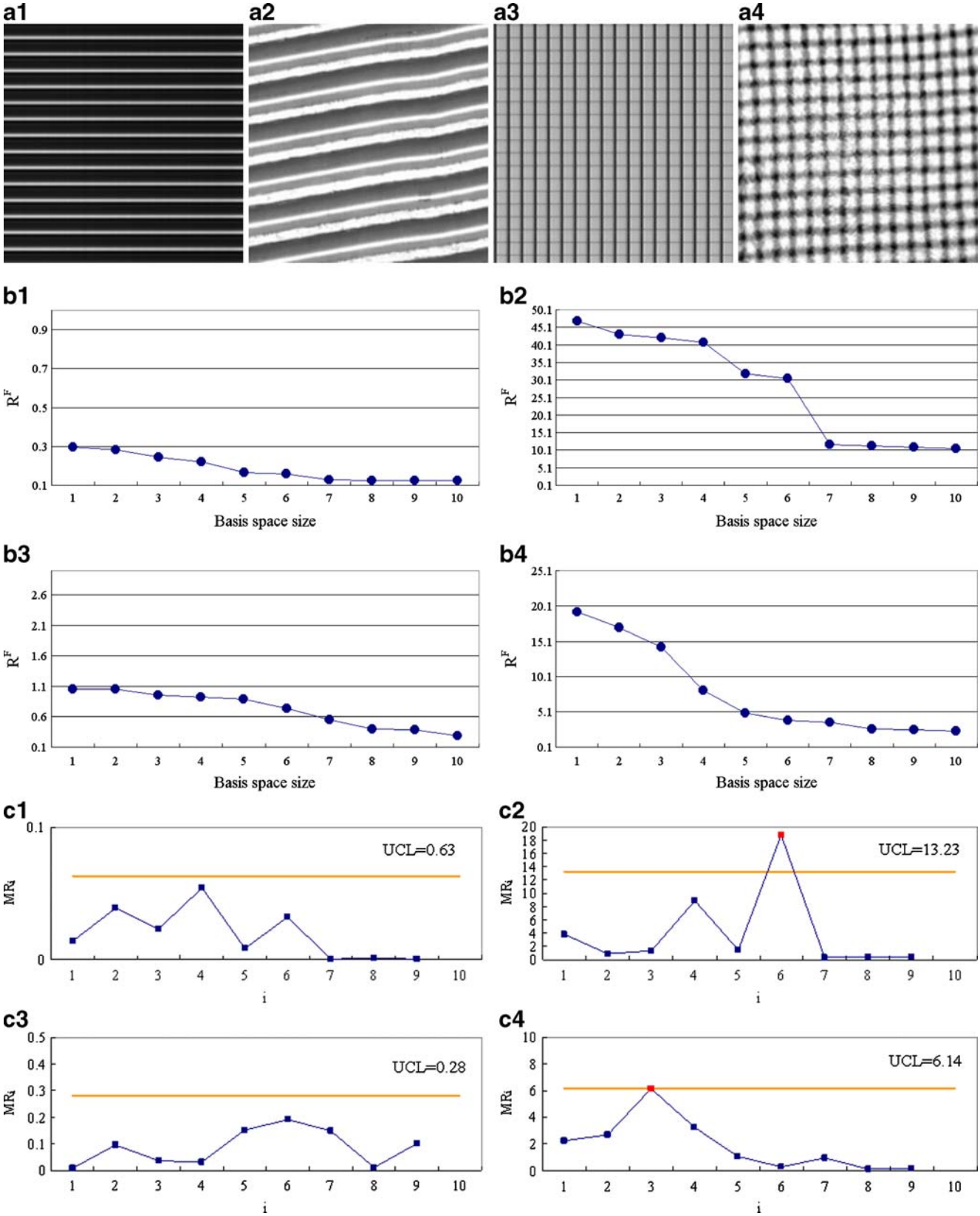

Fig. 5 (*a1–a4*) Nondefective training samples of the OLED, internal thread, PLED, and contact lens dioptric pattern, respectively; (*b1–b4*) residual curves corresponding to (*a1–a4*); and (*c1–c4*) moving range control charts corresponding to (*b1–b4*)

3.2 NMF-based image restoration

As shown in Figs. 1 and 2, the NMF approximation may be regarded as a kind of self-refining scheme that can self-reconstruct a referential golden template of the original directional texture surface. The aim of the surface defect inspection application is to obtain a restored image $\mathbf{X_R}$ to be used in template matching for background texture removal. We initially reconstructed a close approximate texture of the original image, i.e., NMA, by properly selecting the value of k and then highlighting the discrepancies between the original image and the NMA by image subtraction. The above idea can be formulated as,

$$\mathbf{X_R} = \mathbf{X} - \mathrm{NMF}_k(\mathbf{X}) \tag{3}$$

Compared with the available template-matching methods, the proposed scheme does not require a pretraining stage to build up a golden template; it requires only the sample itself without constraint on horizontal and vertical shifting or changes in illumination. These are discussed in detail in Sections 4.2 and 4.3.

3.3 Basis space size

As shown in Fig. 2, underspecification or overspecification of the basis space size definitely distorts the NMA. For this reason, we must select an appropriate value for k in $\mathrm{NMF}_k(\mathbf{X})$ in Eq. 3 that will sufficiently approximate the texture structure so that subtraction can be used to obtain the restored image. However, even once the value of k is selected, there is still the unresolved issue remaining that no optimal rule for NMF decomposition is available. Therefore, the value of k is generally predetermined either empirically by trial and error or though some heuristic approaches. We design a supervised ERC rule to determine the k value that indicates an elbow in the plot of the basis space size as a function of the residual. In general, an elbow signifies the basis space size at which NMF shows its limiting approximation ability for the original image. Below the dimensionality of the elbow point, the residual curve has a steeper slope, which indicates significant improvements due to capturing the most latent organization and structure within the given image. However, above the dimensionality of the elbow point, the residual curve has a flatter slope, which indicates insignificant improvements and waste of computation time. The ERC rule eliminates human intervention for the choice of the proper basis space size for a particular directional texture image. A defect-free training image must be prepared for the ERC rule. Residuals for basis space sizes of 1 to N in increments of 1 are generated first, i.e., $\mathrm{R_1}^{\mathrm{F}}$, $\mathrm{R_2}^{\mathrm{F}}$, …, $\mathrm{R}^{\mathrm{F}}{}_N$. Next, the absolute value of the difference between two consecutive residuals is calculated by

$$\mathrm{MR}_i = \mathrm{R}^{\mathrm{F}}{}_i - \mathrm{R}^{\mathrm{F}}{}_{i+1} \tag{4}$$

where i=1, 2, …, N−1. The physical meaning of MR_i is the residual curvature between $\mathrm{R}^{\mathrm{F}}{}_i$ and $\mathrm{R}^{\mathrm{F}}{}_{i+1}$. The residual curvatures are then fed into a moving range control chart

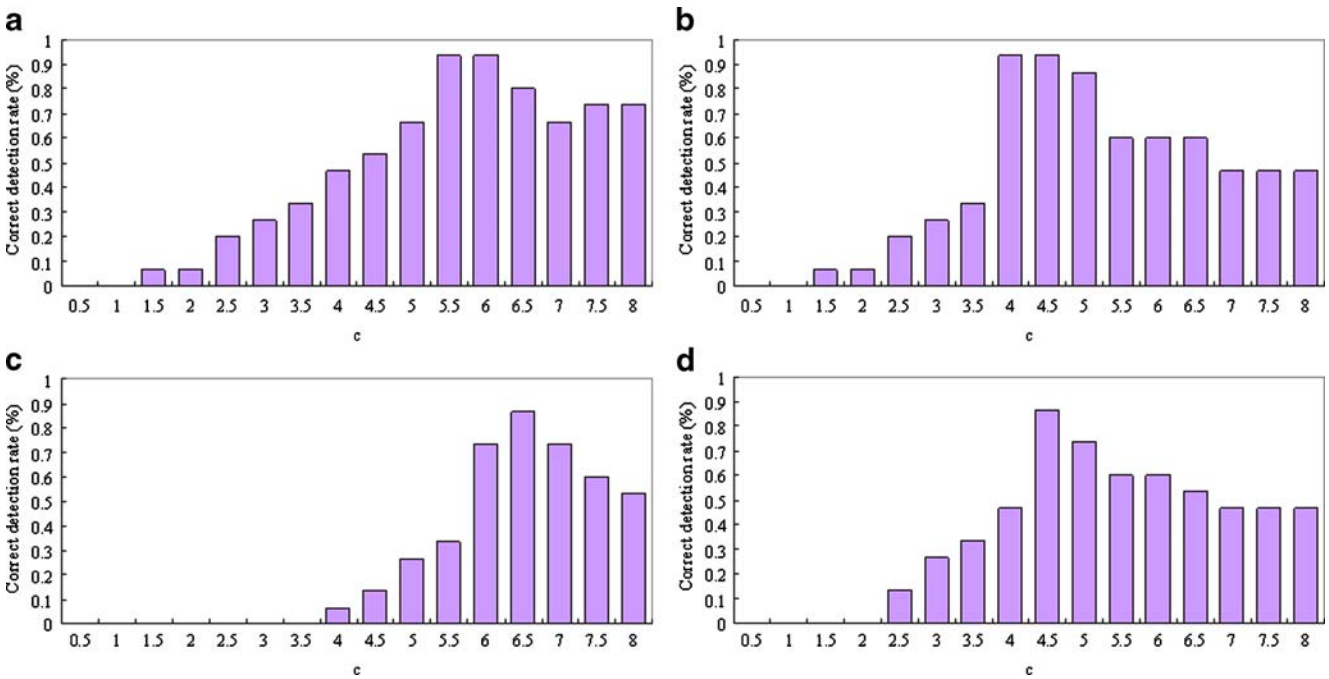

Fig. 6 **a**–**d** Histogram of correct detection rate as a function of c for the OLED, internal thread, PLED, and contact lens dioptric pattern, respectively

that is well suited to individual measurements and tracking the variation of the residual sequences. The upper control limit (UCL) in the moving range control chart is

$$\mathrm{UCL} = 3.267 \times \overline{\mathrm{MR}} \tag{5}$$

where $\overline{\mathrm{MR}}$ is the average of all the residual curvatures. Note that the physical meaning of this moving range control chart procedure is to detect the special cases of the residual curvatures that indicate potential elbows of a residual curve. If no MR_i exists outside the UCL, the shape of the residual curve is very smooth without an elbow. In that case, the basis space size of the image is equal to 1. If only one MR_i exists outside the UCL, then an elbow appears. That is, the residual curve tends to be smooth after $i+1$ and can be used to represent the basis space size for the given image. If more than one MR_i exists outside the UCL, then many elbows appear. That is, the residual curve tends to be smooth after the elbow with the largest index. Finally, the index of the elbow is used as the basis space size in the following inspection stage. However, the proposed scheme is hampered by image rotation because the basis space size for a given defect-free image is determined in a supervised manner. Details of this are discussed in Section 4.4. We used Fig. 1 (a2) as the defect-free training sample and Fig. 2a as the trial defective one. In the training stage, we first decomposed Fig. 1 (a2) to generate NMAs for basis space sizes from 1 to 10. Empirically, $N=10$ was sufficient for a given directional texture surface. As shown in Fig. 1 (b2), we calculated the residual array ($\mathrm{R}^{\mathrm{F}}{}_1$, $\mathrm{R}^{\mathrm{F}}{}_2$, …, $\mathrm{R}^{\mathrm{F}}{}_{10}$) between Fig. 1 (a2) and the ten reconstructed NMAs. Next, a series of residual curvatures (MR_1, MR_2, …, MR_9) was fed into the moving

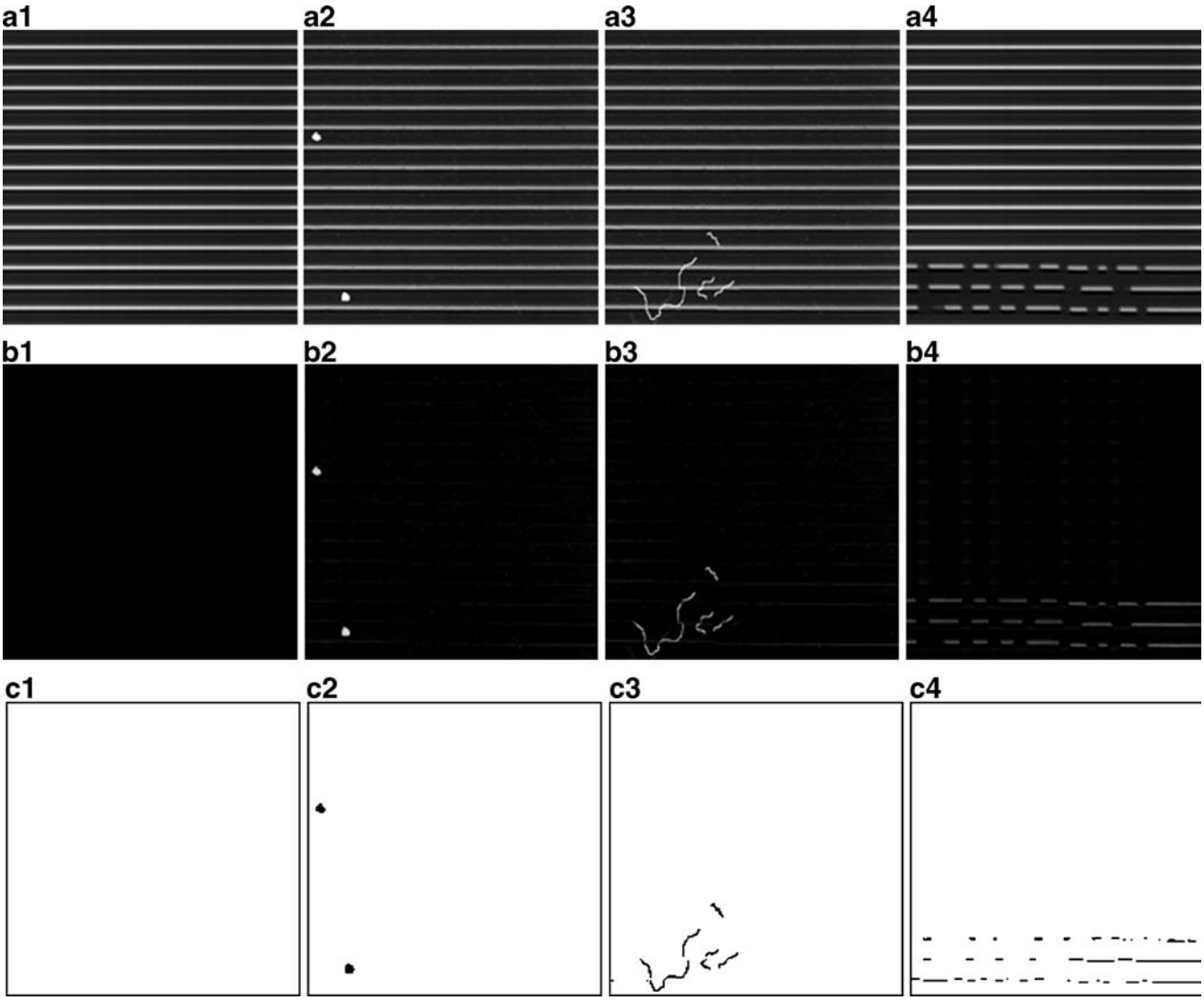

Fig. 7 (*a1–a4*) One nondefective OLED panel and three defective ones with a hole, scratch, and erosion; (*b1–b4*) corresponding restored images; and (*c1–c4*) corresponding binarized images

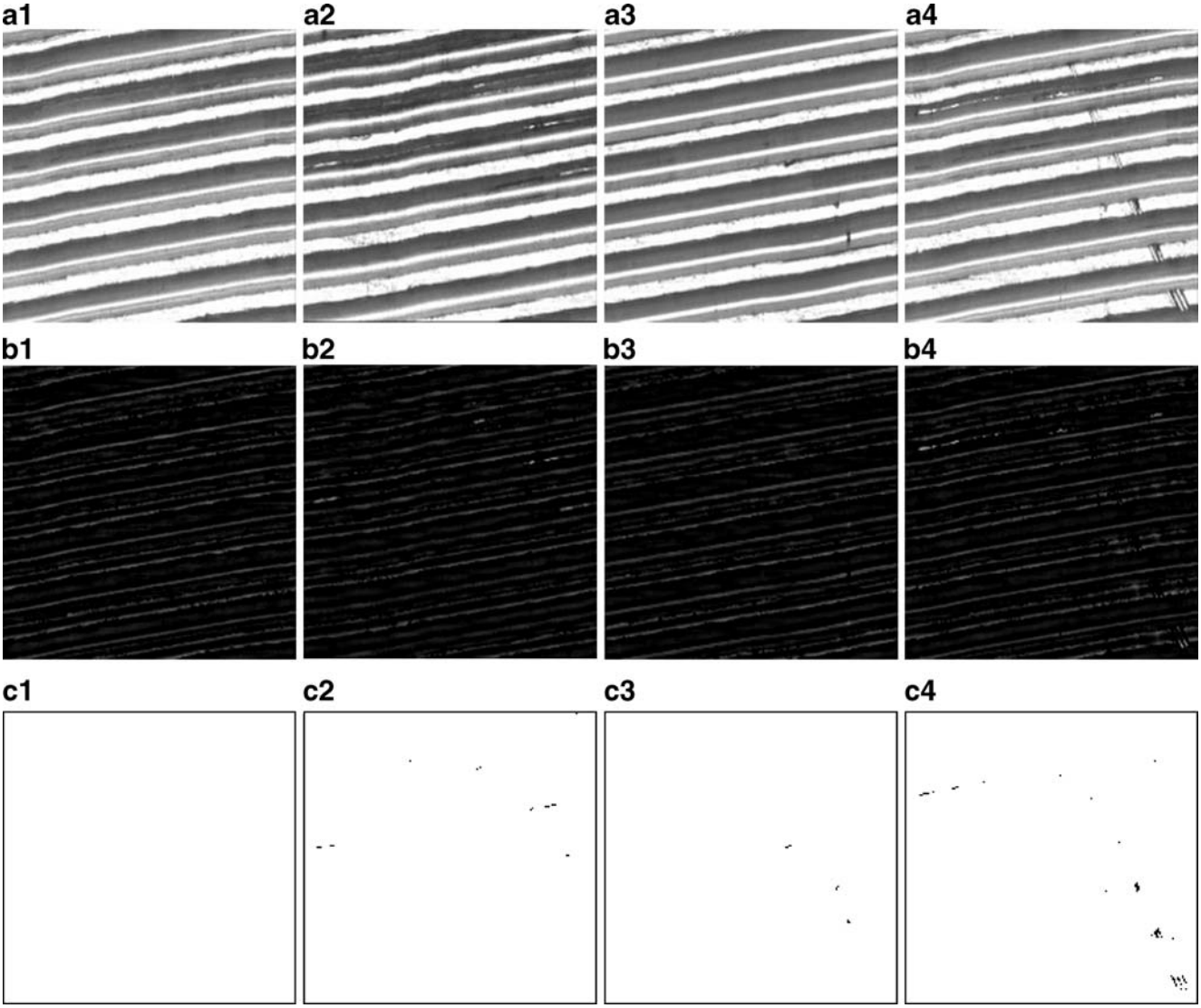

Fig. 8 (*a1–a4*) One nondefective internal thread and three defective ones with a scratch, collapse/flaw, and collapse/scratch; (*b1–b4*) corresponding restored images; and (*c1–c4*) corresponding binarized images

range control chart for elbow detection. In Fig. 3a, MR_2 and MR_4 were outside the UCL and regarded as multielbow cases. The k value of Fig. 1 (a2) was therefore set to 5, i.e., $\mathbf{W}$ of size $m \times 5$ and $\mathbf{H}$ of size $5 \times n$ were sufficient for global texture approximation in the inspection stage. Figure 2f shows the NMA of the trial sample Fig. 2a based on a basis space size equal to 5. Figure 3b shows the corresponding restored image generated from Eq. 3. The global texture was removed or blurred, and the local dark spot defects were distinctly preserved.

3.4 Statistical process control binarization

Since the intensity of the pixels in the restored image has little variation, we can use the statistical process control (SPC) binarization method [3] to establish the upper and lower control limits for highlighting defects. The SPC binarization method can be described by

$$\mathbf{X_B} = \begin{cases} 255 & \text{if } \mu - c \cdot \sigma < \mathbf{X_R} < \mu + c \cdot \sigma \\ 0 & \text{otherwise} \end{cases}. \tag{6}$$

where c is a control constant, and μ and σ are the mean and standard deviation, respectively, of the gray levels of $\mathbf{X_R}$. If a pixel has a gray level that falls between the upper and the lower limits, it is shown as white and is considered to be a texture element that should be removed. Otherwise, it is shown as black and is considered to be a defective element that should be preserved. We examined the effect of three different values of c in Fig. 3b; the results are shown in Fig. 4a–c. Figure 4a gives the binarized result of Fig. 3b for

c=3. We observed that the directional textures were not fully white when the control constant was too small; Fig. 4a contains much noise. Figure 4b gives the binarized result of Fig. 3b for c=5. An appropriate constant control value produced white directional textures and dark defects more precisely. Figure 4b shows the defects clearly. Figure 4c gives the binarized result of Fig. 3b for c=7. We observed that both the directional textures and the defects became white when a large control constant was used. The defects were almost eliminated in Fig. 4c.

We select the parameter c in Eq. 6 in another training stage after determining the appropriate value of k. A set of training images with approximately equal numbers of defective and defect-free samples must be prepared. The confusion matrices are then recorded to determine the number of correct and incorrect detections in a supervised manner for various values of c. Finally, the c value with highest correct detection rate is selected.

The detailed procedure of the proposed scheme is summarized as follows.

Training k:

01 Input a defect-free training image $\mathbf{X_T}$;
02 Generate the first ten residuals: $R^F_i = \|\mathbf{X_T} - NMF_i(\mathbf{X_T})\|^2_F$, $i = 1, 2, \ldots, 10$;
03 Calculate the residual curvatures: $MR_i = R^F_i - R^F_{i+1}$, $i = 1, 2, \ldots, 9$;
04 Feed the residual curvatures into moving range control chart for elbow detection;

Training c:

01 Input M defect-free and defective testing images $\{\mathbf{X_{Ti}}\}$ with closely balanced sample size and the corresponding supervised class labels; fix the k value;
02 **FOR** i = 1 to M
03 Global texture approximation: $NMF_k(\mathbf{X_{Ti}})$;
04 Global texture removal: $\mathbf{X_{Ri}} = \mathbf{X_{Ti}} - NMF_k(\mathbf{X_{Ti}})$;
05 **FOR** j = 0.5 to 8.0 with step of 0.5
06 Local defects extraction: $\mathbf{X_{Bi}} = 255$, if $\mu - j \times \sigma < \mathbf{X_{Ri}} < \mu + j \times \sigma$; $\mathbf{X_{Bi}} = 0$, otherwise;
07 Update the confusion matrix: $\mathbf{C}_j$;
08 **ENDFOR**
09 **ENDFOR**
10 $c = j$, if $\max_j (\text{trace}(\mathbf{C}_j)/M)$;

Inspecting:

01 Input inspected image $\mathbf{X_I}$; fix the k and c values;
02 Global texture approximation: $NMF_k(\mathbf{X_I})$;
03 Global texture removal: $\mathbf{X_R} = \mathbf{X_I} - NMF_k(\mathbf{X_I})$;
04 Local defects extraction: $\mathbf{X_B} = 255$, if $\mu - c \times \sigma < \mathbf{X_R} < \mu + c \times \sigma$; $\mathbf{X_B} = 0$, otherwise.

4 Experiment results

In Section 4.1, we implemented the proposed scheme and conducted experiments to evaluate its performance in detecting defects for different product surfaces which were imaged with size 180×180. Several types of directional texture patterns with defective or defect-free samples were used, including the organic light-emitting diode (OLED) panel, the internal thread, the polymer light-emitting diode (PLED) panel, and the contact lens dioptric pattern. In Sections 4.2 to 4.4, some preliminary and quantitative experiments were also conducted to demonstrate the effects on the proposed scheme of shifting, illumination changes, and image rotation. Furthermore, a sensitivity analysis of the parameters k and c is given in Section 4.5. The inspection algorithm was implemented on AMD Athlon 64 X2 dual-core processor 3600+ (2.01FHZ) PC with 2GB RAM and was programmed by MATLAB in which the ANLSPG source code for NMF learning was adopted from [26] in which the tolerance for a relative stopping condition

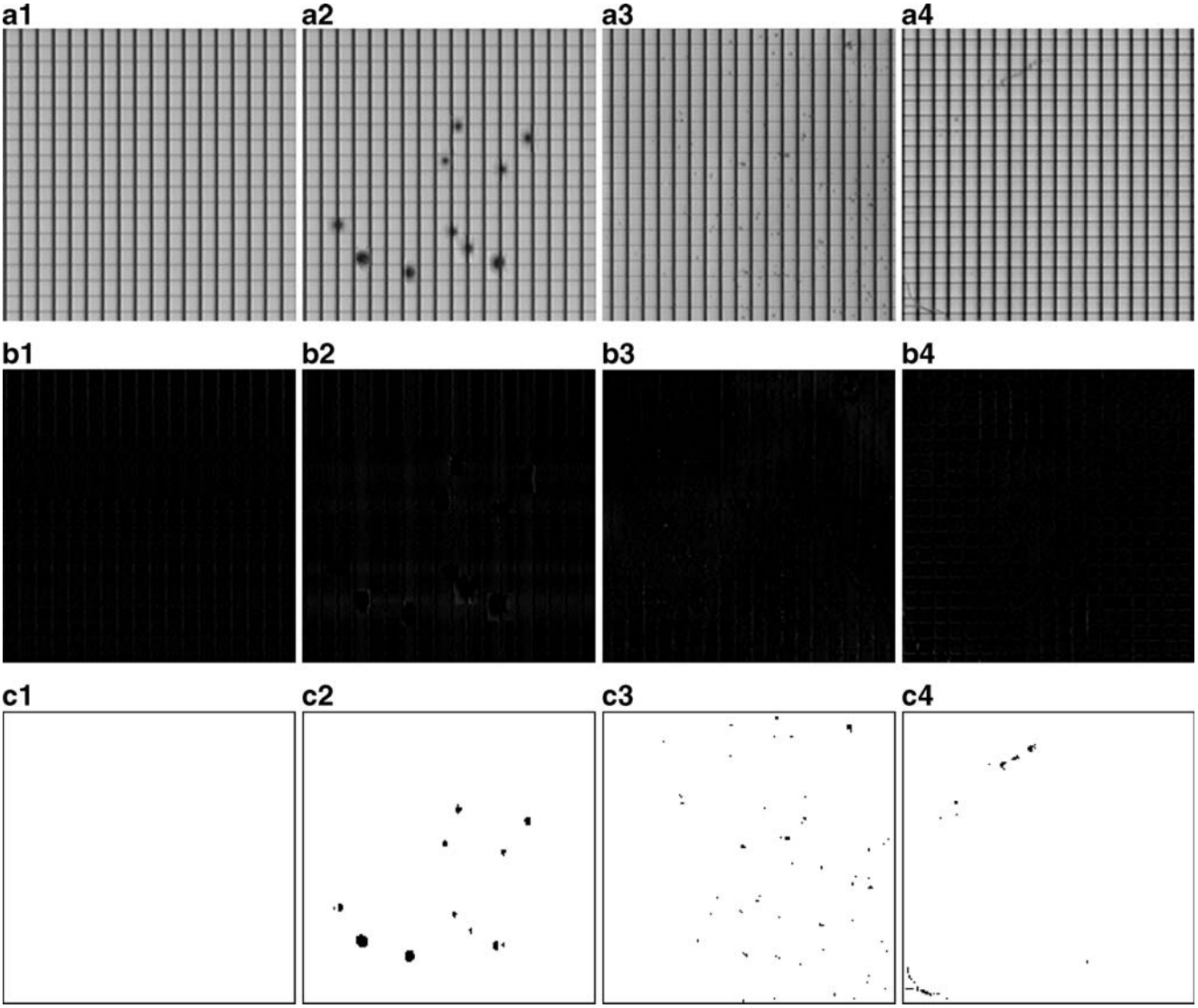

Fig. 9 (*a1–a4*) One nondefective PLED panel and three defective ones with a dark point, particle, and scratch; (*b1–b4*) corresponding restored images; and (*c1–c4*) corresponding binarized images

and the limit of iterations were set as 0.00001 and 500, respectively.

4.1 Directional texture surface inspection

For the k training stage, we prepared four defect-free training images with distinct directional texture; these are shown in Fig. 5 (a1–a4) as follows: an OLED panel with a periodic unidirectional line structure in Fig. 5 (a1); an internal thread with a periodic, unidirectional, and rotational line structure in Fig. 5 (a2); a PLED panel with a periodic and orthogonal line structure in Fig. 5 (a3); and a contact lens dioptric pattern with a periodic, orthogonal, and rotational line structure in Fig. 5 (a4). The corresponding residual curves are shown in Fig. 5 (b1–b4), and the related corresponding moving range control charts are shown in Fig. 5 (c1–c4). As shown in Fig. 5 (c1 and c3), there was no residual curvature outside the UCL, which means that no elbow appeared. Thus, both the OLED and PLED panel could be approximated well by only $NMF_1(\mathbf{X})$. In Fig. 5 (c2 and c4), one of the residual curvatures was outside the UCL, which means that the residual curve did have an elbow. This was because a rotated directional texture always needs a larger basis space size to represent the latent structure. The elbow in Fig. 5 (c2) was equal to 6, so the internal thread was approximated by $NMF_7(\mathbf{X})$. The elbow in Fig. 5 (c4) was equal to 3, so the contact lens dioptric pattern was approximated by $NMF_4(\mathbf{X})$.

After obtaining the k value of each training sample in Fig. 5 (a1–a4), we prepared another 15 individual training samples (seven defect-free and eight defective samples) to determine the c value. As shown in Fig. 6a–d, we recorded

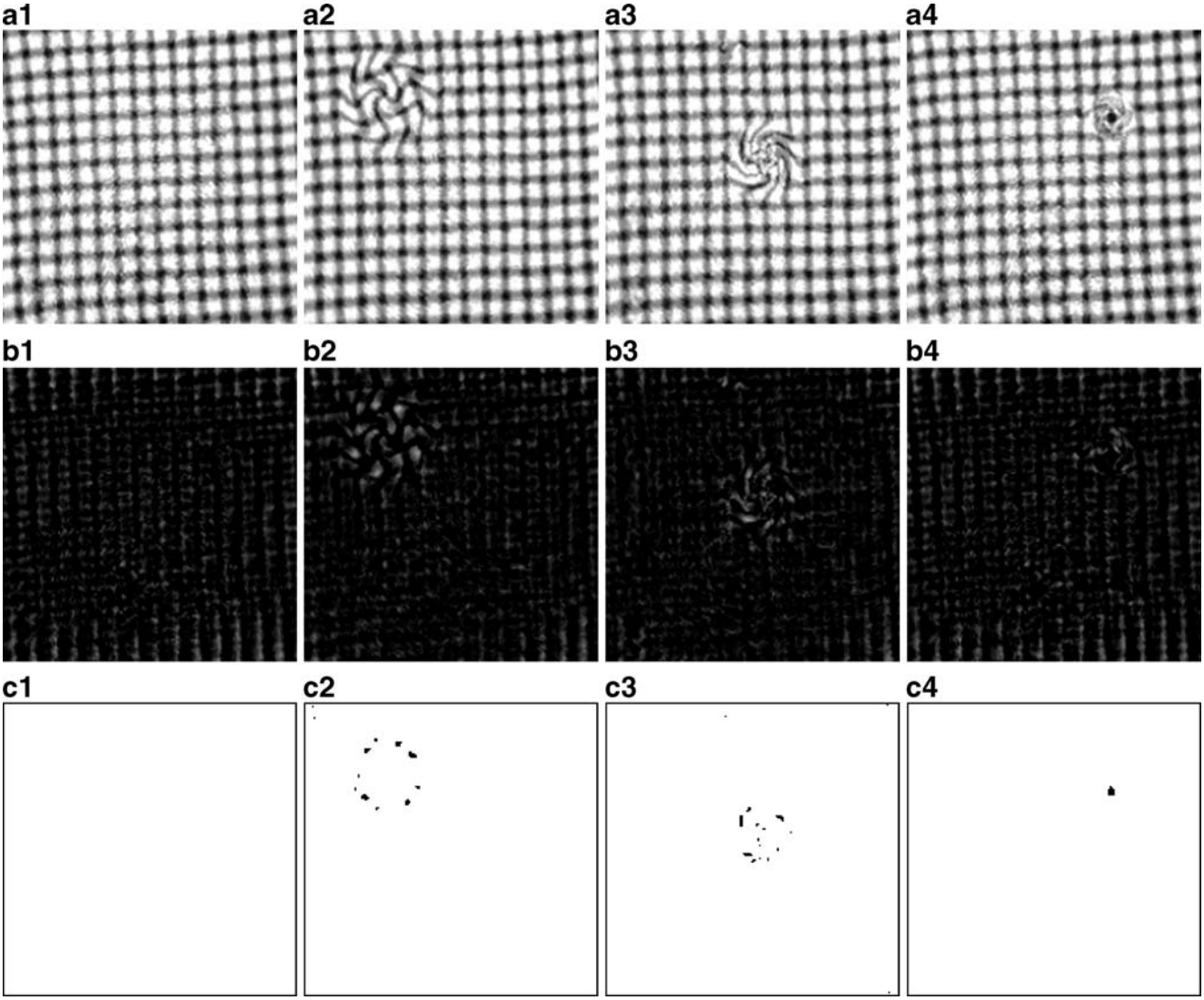

Fig. 10 (*a1–a4*) One nondefective contact lens dioptric pattern and three defective ones with a twist, eddy, and dark point; (*b1–b4*) corresponding restored images; and (*c1–c4*) corresponding binarized images

the corresponding number of correct detections in a supervised manner for c=0.5, 1.0, …, 8.0 using histograms. The highest bar of the histogram was chosen as the individual optimal c. (In the case where there was more than one highest bar, the smallest value of c was selected.) In other words, we set c=5.5, 4.0, 6.5, and 4.5, respectively, for the OLED, the internal thread, the PLED, and the contact lens dioptric pattern in the SPC binary formulas.

After the above k and c training stages, we tested some images for defect inspection. Figures 7 (a1–a4), 8 (a1–a4), 9 (a1–a4), and 10 (a1–a4), respectively, show one defect-free and three defective product surfaces with distinctly different defects. Figures 7 (b1–b4), 8 (b1–b4), 9 (b1–b4), and 10 (b1–b4) show the corresponding images restored by the NMF-based image restoration scheme with k=1, 7, 1, and 4, respectively. Note that the directional textures of these product surfaces were almost eliminated. Figures 7 (c1–c4), 8 (c1–c4), 9 (c1–c4), and 10 (c1–c4) show the corresponding images binarized by SPC binarization with c= 5.5, 4.0, 6.5, and 4.5. Note that Figs. 7 (c1), 8 (c1), 9 (c1), 10 (c1) show a clear response; Figs. 7 (c2–c4), 8 (c2–c4), 9

Table 1 The quantitative inspection results on different products

Products Items	OLED	Internal thread	PLED	Contact lens dioptric pattern
Sample size	30	40	30	50
Inspection rate (%)	93.33	92.50	93.33	92.00
Average inspection time of an image (sec.)	0.124	0.927	0.141	0.754

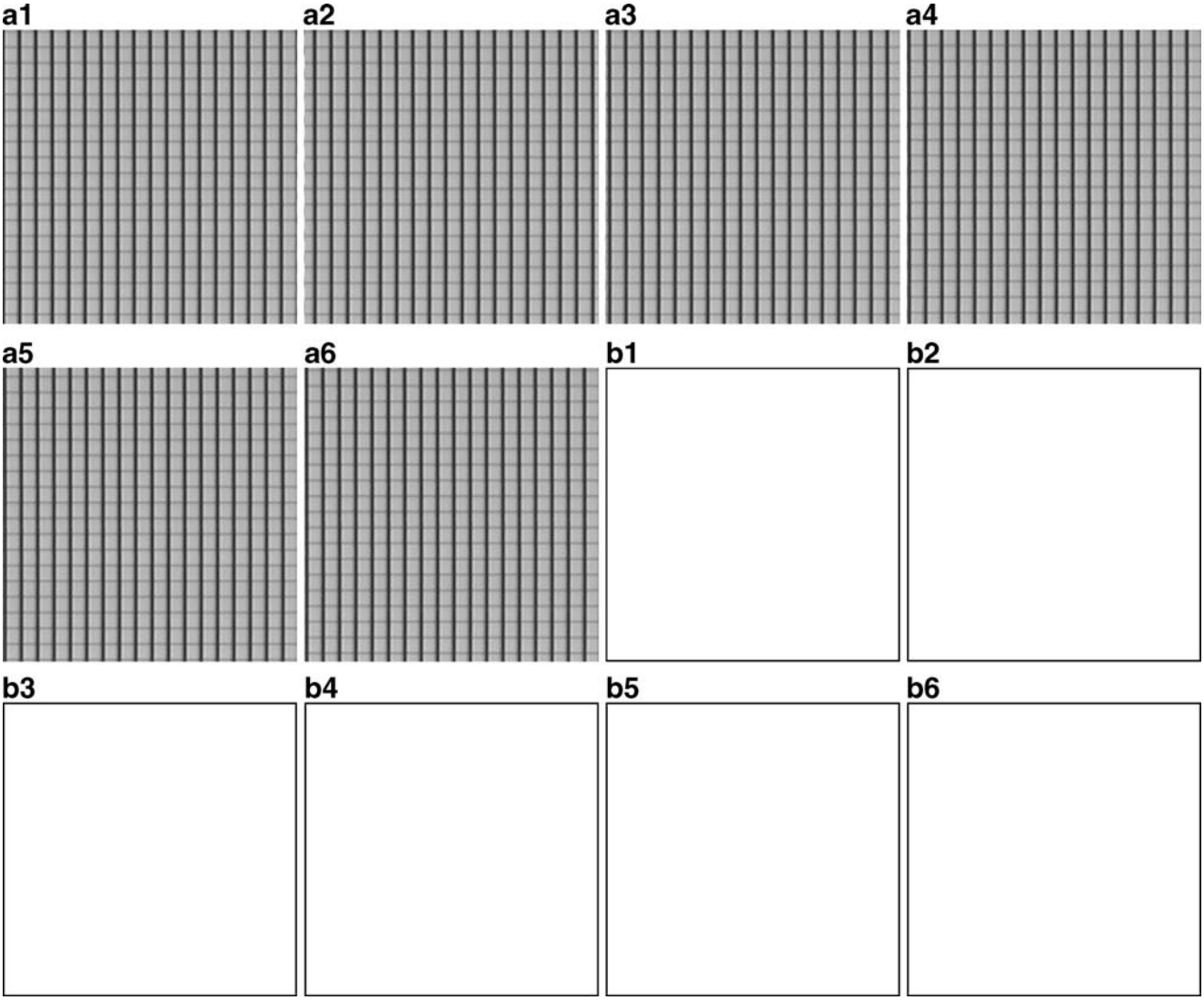

Fig. 11 (*a1–a3*) and (*a4–a6*) horizontal and vertical shifting versions of Fig. 9 (a1) by 1-, 5-, and 9-pixel(s); and (*b1–b3*) and (*b4–b6*) corresponding binarized images

(c2–c4), and 10 (c2–c4) show the defects that were initially embedded in these product surfaces.

A number of samples were used for evaluating the accuracy and time of defect detection of the proposed scheme including 30 OLEDs, 40 internal threads, 30 PLEDs, and 50 contact lenses; half of each kind of samples is defect-free while the other half is with defect. The quantitative data on different products were summarized in Table 1. The successful inspection rate of each kind of product, respectively, was up to 93.33%, 92.50%, 93.33%, and 92.00%. It took less than 1 s to inspect an image of each kind of sample. The larger the basis space size (k) is, the longer the learning time of NMA will be. All of the above experiments demonstrated that the proposed scheme can detect the defects on directional textures accurately, efficiently, and robustly.

4.2 Effect of the image shifting

We evaluated the effect of the proposed NMF-based image restoration scheme under varying shifting conditions. Illustrated samples for this experiment were taken from Fig. 9 (a1 and a2). Because the PLED is composed with 10×10 rectangular pattern, we only tested the proposed scheme on 1, 5, and 9 pixel(s) vertical or horizontal shifting versions (shown in Fig. 11 (a1–a6) and Fig. 12 (a1–a6), respectively) with the fixed parameters $k=1$ and $c=6.5$. As shown in the corresponding Figs. 11 (b1–b6) and 12 (b1–b6), the proposed scheme produced clear results and highlighted defects on the surfaces, regardless of the amount of shifting, because of the self-reference golden template generation discussed in Section 3.2.

We tested all samples of different products, mentioned in Section 4.1, by randomly shifting the image. The quanti-

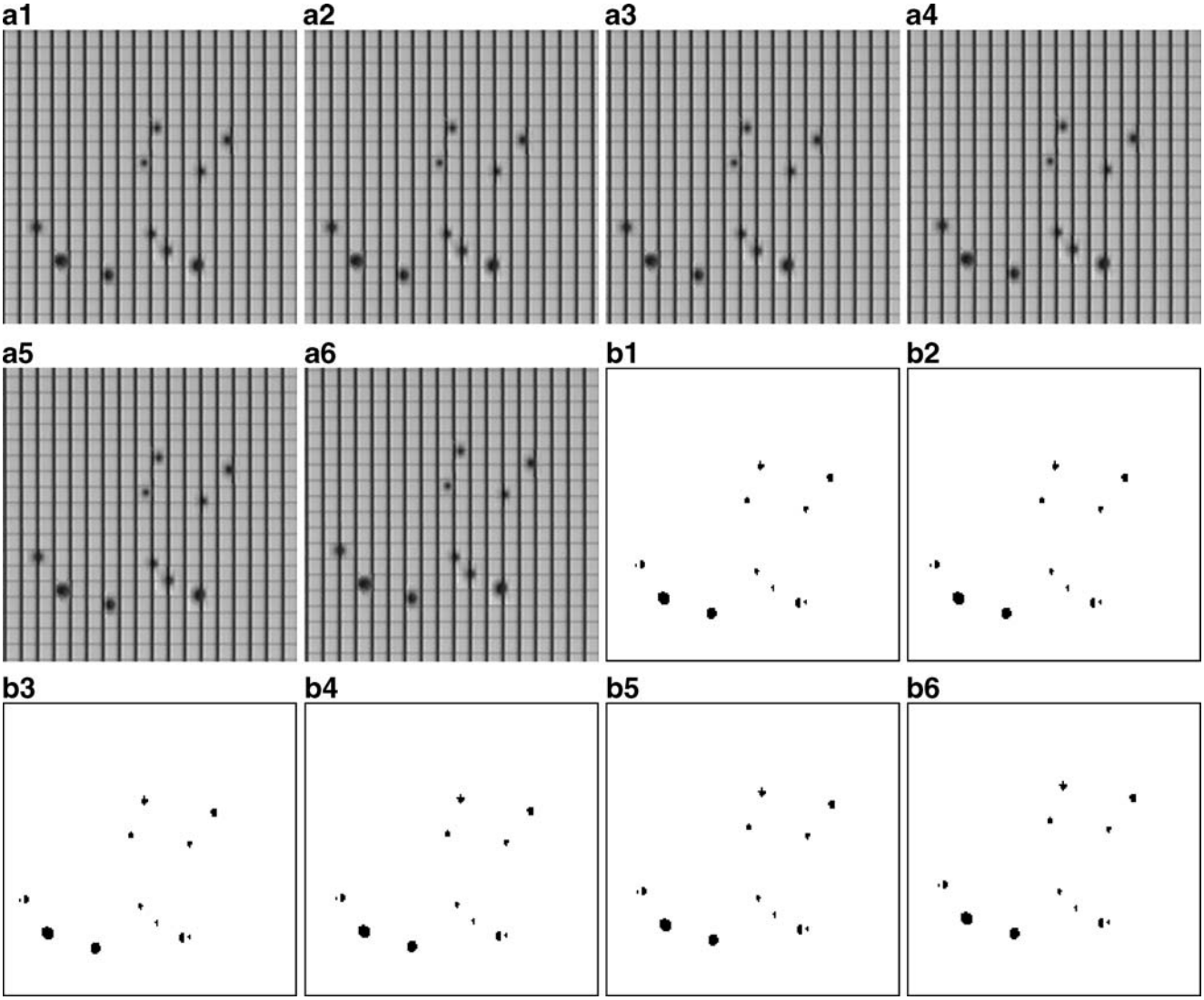

Fig. 12 (*a1–a3*) and (*a6–a10*) horizontal and vertical shifting versions of Fig. 9 (a2) by 1-, 5-, and 9-pixel(s); and (*b1–b3*) and (*b4–b6*) corresponding binarized images

tative data of the shifting experiments were summarized in Table 2. The successful inspection rate of the four kinds of products was up to 93.33%, 92.50%, 93.33%, and 92.00%, respectively, which was the same as Table 1. This confirms that the proposed scheme is invariant to horizontal and vertical shifting.

4.3 Effect of the changes in illumination

We evaluated the effect of the proposed NMF-based image restoration scheme under varying illumination conditions. Illustrated samples for this experiment were taken from Fig. 9 (a1 and a2), for which some illumination changes are

Table 2 The quantitative inspection results on different products with varying shifting, illumination, or rotation conditions

Products Items	OLED	Internal thread	PLED	Contact lens dioptric pattern
Sample size	30	40	30	50
Inspection rate of the shifting images (%)	93.33	92.50	93.33	92.00
Inspection rate of the illumination changed images (%)	93.33	92.50	93.33	92.00
Inspection rate of the rotated images (%)	50.00	50.00	50.00	50.00

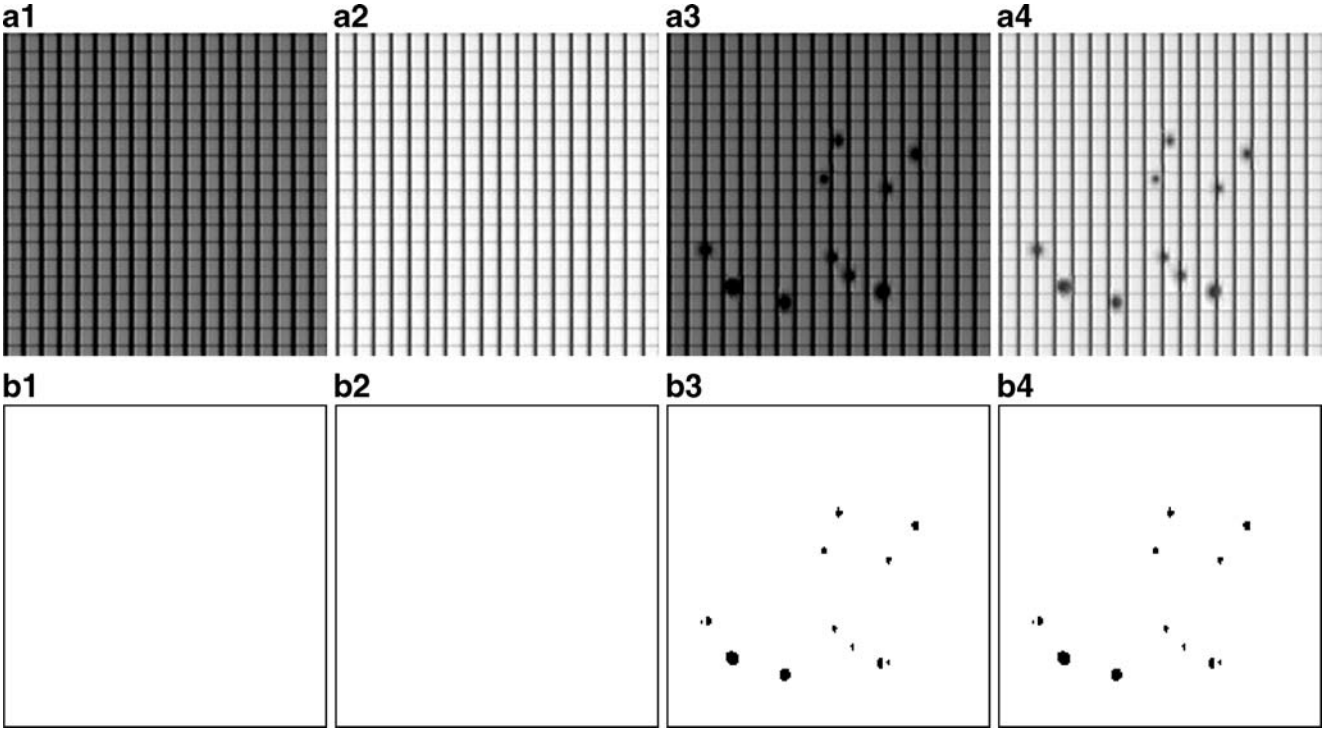

Fig. 13 (*a1*, *a2*) and (*a3*, *a4*) are Figs. 9 (a1) and 9 (a2), respectively, with relatively darker and brighter illumination; and (*b1–b4*) are the corresponding binarized images

shown in Fig. 13 (a1, a2 and a3, a4, respectively). We tested the proposed scheme on those images with the fixed parameters k=1 and c=6.5. As shown in the corresponding Fig. 13 (b1–b4), the proposed scheme produced clear results and highlighted defects on the surfaces even if the optimal parameters k and c were determined under a specific illumination level. The NMF adaptively learned two submatrices to reconstruct an NMA whose latent structure (including shape and intensity) was very similar to the original image.

We tested all samples of different products, mentioned in Section 4.1, by randomly changing the image illumination. The quantitative data of the illumination experiments were summarized in Table 2. The successful inspection rate of the four kinds of products was up to 93.33%, 92.50%, 93.33%, and 92.00%, respectively, which was the same as Table 1. This confirms that the proposed scheme was invariant to changing illumination.

4.4 Effect of the image rotation

We evaluated the effect of the proposed NMF-based image restoration scheme for varying image rotations. For this experiment, Fig. 14 (a1, a2 and a3, a4) was obtained by rotating Fig. 9 (a1 and a2) by 9° and 18°, respectively. We then applied the proposed scheme to the images with the fixed parameters k=1 and c=6.5. Many undesirable textures remained in the restored images, as shown in Fig. 14 (b1 and b2). Those preserved textures were then eliminated by SPC binarization in the binarized images of Fig. 14 (c1 and c2). Superficially, image rotation seemed not to cause any problems for defect-free samples. In fact, the "pass claims" in Fig. 14 (c1 and c2) should be regarded as spurious correct results due to the high intensity and high contrast in Fig. 14 (b1 and b2) that yielded large mean and standard deviation values and relaxed the control limits for Eq. 6. Consequently, the intensities of remaining texture in Fig. 14 (b1 and b2) were fortunately classified as removable elements. As shown in Fig. 14 (b3 and b4), not only the undesirable texture but also the dark point defects remained in the restored images. All of them were then eliminated in Fig. 14 (c3 and c4). The pass claims of Fig. 14 (c3 and c4) should be regarded as missed detections for a reason similar to that of the preceding defect-free case. Consequently, the intensities of dark points in Fig. 14 (b3 and b4) were also unfortunately classified as removable elements.

We tested all samples of different products, mentioned in Section 4.1, by randomly rotating the image. The quantitative data of the rotation experiments were summarized in Table 2. The successful inspection rate of the four kinds of products was degraded to 50.00% which was dramatically

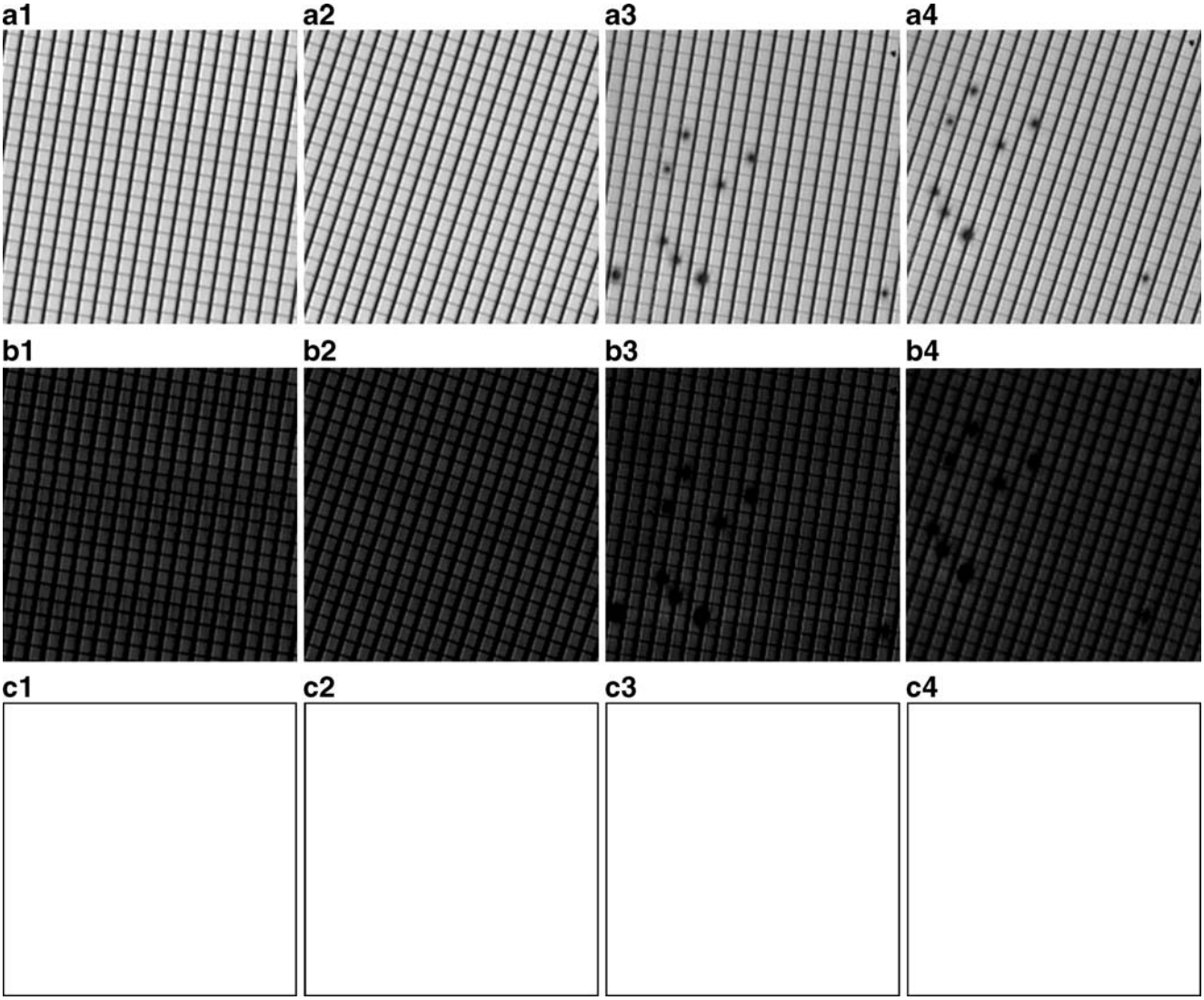

Fig. 14 (*a1*, *a2*) and (*a3*, *a4*) are Figs. 9 (a1) and (a2), respectively, with rotations of 9° and 18°; (*b1–b4*) are the corresponding restored images; and (*c1–c4*) are the corresponding binarized images

distinct with that given in Table 1. Thus, based on the results from Fig. 14 and Table 2, we found that the proposed scheme was sensitive to image rotation.

4.5 The sensitivity analysis of the parameters *k* and *c*

We further demonstrated the sensitivity analysis of the parameters *k* and *c* of each kind of sample. In order to give more informative data, we separately recorded the correct inspection rates based on defective-free and defective samples. The former was listed in the top of each cell, while the latter was listed at the bottom of each cell in Tables 3, 4, 5, and 6. The suggested combinations of (*k*, *c*) were marked in italics. In terms of this experiment, the concluding remarks about the parameters effect on the inspection results of defect-free and defective samples were summarized in Table 7.

5 Conclusions and discussions

We have described a new global NMF-based image restoration scheme for detecting defects in directional textures. The scheme first determines the latent structure of a given directional texture by making a good approximation. The texture then becomes a uniform gray level by subtracting the original image from the NMA. The texture is removed in the binarized image while any original defects are distinctly preserved. A nondefective directional texture surface image resulted in a clear response in our experiments; otherwise, distinct defects were clearly indicated with rough shapes and actual locations. This demonstrated the ability of the proposed scheme to detect defects in surfaces with various periodic patterns.

Experiments showed that the proposed scheme was insensitive to horizontal and vertical shifting and changes

Table 3 The parameters k and c vs. inspection rate (%) of the OLEDs

c / k	0.5	1.0	1.5	2.0	2.5	3.0	3.5	4.0	4.5	5.0	5.5	6.0	6.5	7.0	7.5	8.0
1	0.0	0.0	0.0	0.0	0.0	0.0	0.0	26.7	86.7	100.0	*100.0*	*100.0*	100.0	100.0	100.0	100.0
	0.0	0.0	0.0	0.0	0.0	6.7	13.3	20.0	46.7	60.0	*86.7*	*86.7*	80.0	80.0	66.7	60.0
2	0.0	0.0	0.0	0.0	0.0	0.0	0.0	26.7	86.7	100.0	100.0	100.0	100.0	100.0	100.0	100.0
	0.0	0.0	0.0	0.0	0.0	0.0	13.3	13.3	20.0	20.0	26.7	40.0	40.0	53.3	53.3	46.7
3	0.0	0.0	0.0	0.0	0.0	0.0	0.0	13.3	80.0	100.0	100.0	100.0	100.0	100.0	100.0	100.0
	0.0	0.0	0.0	0.0	0.0	0.0	13.3	13.3	20.0	20.0	26.7	40.0	40.0	46.7	46.7	40.0
4	0.0	0.0	0.0	0.0	0.0	0.0	0.0	0.0	73.3	80.0	86.7	100.0	100.0	100.0	100.0	100.0
	0.0	0.0	0.0	0.0	0.0	0.0	13.3	13.3	13.3	20.0	20.0	20.0	33.3	40.0	33.3	33.3
5	0.0	0.0	0.0	0.0	0.0	0.0	0.0	0.0	46.7	80.0	86.7	93.3	100.0	100.0	100.0	100.0
	0.0	0.0	0.0	0.0	0.0	0.0	13.3	13.3	13.3	20.0	20.0	20.0	26.7	26.7	20.0	20.0
6	0.0	0.0	0.0	0.0	0.0	0.0	0.0	0.0	40.0	80.0	86.7	93.3	100.0	100.0	100.0	100.0
	0.0	0.0	0.0	0.0	0.0	0.0	13.3	13.3	13.3	20.0	20.0	20.0	13.3	13.3	6.7	6.7
7	0.0	0.0	0.0	0.0	0.0	0.0	0.0	0.0	40.0	73.3	86.7	93.3	100.0	100.0	100.0	100.0
	0.0	0.0	0.0	0.0	0.0	0.0	0.0	6.7	6.7	13.3	13.3	13.3	13.3	13.3	6.7	6.7
8	0.0	0.0	0.0	0.0	0.0	0.0	0.0	0.0	40.0	73.3	86.7	93.3	100.0	100.0	100.0	100.0
	0.0	0.0	0.0	0.0	0.0	0.0	0.0	6.7	6.7	6.7	13.3	6.7	6.7	0.0	0.0	0.0
9	0.0	0.0	0.0	0.0	0.0	0.0	0.0	0.0	40.0	73.3	86.7	93.3	100.0	100.0	100.0	100.0
	0.0	0.0	0.0	0.0	0.0	0.0	0.0	0.0	6.7	6.7	6.7	6.7	0.0	0.0	0.0	0.0
10	0.0	0.0	0.0	0.0	0.0	0.0	0.0	0.0	40.0	73.3	86.7	93.3	100.0	100.0	100.0	100.0
	0.0	0.0	0.0	0.0	0.0	0.0	0.0	0.0	6.7	6.7	6.7	0.0	0.0	0.0	0.0	0.0

Table 4 The parameters k and c vs. inspection rate (%) of the internal threads

c / k	0.5	1.0	1.5	2.0	2.5	3.0	3.5	4.0	4.5	5.0	5.5	6.0	6.5	7.0	7.5	8.0
1	0.0	0.0	0.0	100.0	100.0	100.0	100.0	100.0	100.0	100.0	100.0	100.0	100.0	100.0	100.0	100.0
	0.0	0.0	0.0	0.0	0.0	5.0	0.0	0.0	0.0	0.0	0.0	0.0	0.0	0.0	0.0	0.0
2	0.0	0.0	0.0	0.0	70.0	100.0	100.0	100.0	100.0	100.0	100.0	100.0	100.0	100.0	100.0	100.0
	0.0	0.0	0.0	0.0	0.0	5.0	0.0	0.0	0.0	0.0	0.0	0.0	0.0	0.0	0.0	0.0
3	0.0	0.0	0.0	0.0	30.0	100.0	100.0	100.0	100.0	100.0	100.0	100.0	100.0	100.0	100.0	100.0
	0.0	0.0	0.0	0.0	0.0	5.0	0.0	0.0	0.0	0.0	0.0	0.0	0.0	0.0	0.0	0.0
4	0.0	0.0	0.0	0.0	0.0	45.0	100.0	100.0	100.0	100.0	100.0	100.0	100.0	100.0	100.0	100.0
	0.0	0.0	0.0	0.0	0.0	25.0	40.0	15.0	10.0	5.0	5.0	0.0	0.0	0.0	0.0	0.0
5	0.0	0.0	0.0	0.0	0.0	15.0	75.0	100.0	100.0	100.0	100.0	100.0	100.0	100.0	100.0	100.0
	0.0	0.0	0.0	0.0	0.0	25.0	40.0	15.0	10.0	5.0	5.0	0.0	0.0	0.0	0.0	0.0
6	0.0	0.0	0.0	0.0	0.0	0.0	35.0	90.0	100.0	100.0	100.0	100.0	100.0	100.0	100.0	100.0
	0.0	0.0	0.0	0.0	0.0	0.0	30.0	55.0	30.0	10.0	5.0	0.0	0.0	0.0	0.0	0.0
7	0.0	0.0	0.0	0.0	0.0	0.0	0.0	85.0	*95.0*	100.0	100.0	100.0	100.0	100.0	100.0	100.0
	0.0	0.0	0.0	0.0	0.0	0.0	15.0	90.0	*90.0*	75.0	55.0	5.0	5.0	0.0	0.0	0.0
8	0.0	0.0	0.0	0.0	0.0	0.0	0.0	50.0	90.0	100.0	100.0	100.0	100.0	100.0	100.0	100.0
	0.0	0.0	0.0	0.0	0.0	0.0	15.0	60.0	70.0	65.0	55.0	5.0	5.0	0.0	0.0	0.0
9	0.0	0.0	0.0	0.0	0.0	0.0	0.0	35.0	65.0	100.0	100.0	100.0	100.0	100.0	100.0	100.0
	0.0	0.0	0.0	0.0	0.0	0.0	0.0	30.0	60.0	55.0	55.0	5.0	5.0	0.0	0.0	0.0
10	0.0	0.0	0.0	0.0	0.0	0.0	0.0	15.0	50.0	90.0	100.0	100.0	100.0	100.0	100.0	100.0
	0.0	0.0	0.0	0.0	0.0	0.0	0.0	20.0	50.0	50.0	40.0	5.0	5.0	0.0	0.0	0.0

Table 5 The parameters k and c vs. inspection rate (%) of the PLEDs

c / k	0.5	1.0	1.5	2.0	2.5	3.0	3.5	4.0	4.5	5.0	5.5	6.0	6.5	7.0	7.5	8.0
1	0.0	0.0	0.0	0.0	0.0	0.0	0.0	0.0	0.0	0.0	0.0	13.3	*100.0*	100.0	100.0	100.0
	0.0	0.0	0.0	0.0	13.33	13.33	13.33	20.0	33.3	40.0	73.3	86.7	*86.7*	80.0	53.3	40.0
2	0.0	0.0	0.0	0.0	0.0	0.0	0.0	0.0	0.0	0.0	0.0	13.3	86.7	86.7	100.0	100.0
	0.0	0.0	0.0	0.0	13.3	13.3	13.3	20.3	26.7	40.0	73.3	80.0	86.7	66.7	46.7	40.0
3	0.0	0.0	0.0	0.0	0.0	0.0	0.0	0.0	0.0	0.0	0.0	0.0	80.0	80.0	100.0	93.3
	0.0	0.0	0.0	0.0	13.3	13.3	13.3	20.3	26.7	40.0	53.3	73.3	80.0	60.0	46.7	33.3
4	0.0	0.0	0.0	0.0	0.0	0.0	0.0	0.0	0.0	0.0	0.0	0.0	46.7	53.3	53.3	80.0
	0.0	0.0	0.0	0.0	13.3	13.3	13.3	13.3	26.7	33.3	46.7	73.3	66.7	46.7	40.0	26.7
5	0.0	0.0	0.0	0.0	0.0	0.0	0.0	0.0	0.0	0.0	0.0	0.0	46.7	46.7	53.3	66.7
	0.0	0.0	0.0	0.0	13.3	13.3	13.3	13.3	20.0	20.0	33.3	40.0	40.0	33.3	20.0	20.0
6	0.0	0.0	0.0	0.0	0.0	0.0	0.0	0.0	0.0	0.0	0.0	0.0	33.3	40.0	53.3	60.0
	0.0	0.0	0.0	0.0	6.7	6.7	6.7	6.7	13.3	20.0	33.3	40.0	40.0	26.7	20.0	20.0
7	0.0	0.0	0.0	0.0	0.0	0.0	0.0	0.0	0.0	0.0	0.0	0.0	20.0	26.7	33.3	40.0
	0.0	0.0	0.0	0.0	6.7	6.7	6.7	6.7	6.7	20.0	33.3	33.3	33.3	26.7	20.0	13.3
8	0.0	0.0	0.0	0.0	0.0	0.0	0.0	0.0	0.0	0.0	0.0	0.0	6.7	20.0	33.3	40.0
	0.0	0.0	0.0	0.0	0.0	0.0	0.0	0.0	0.0	13.3	26.7	33.3	33.3	20.0	13.3	13.3
9	0.0	0.0	0.0	0.0	0.0	0.0	0.0	0.0	0.0	0.0	0.0	0.0	0.0	13.3	26.7	33.3
	0.0	0.0	0.0	0.0	0.0	0.0	0.0	0.0	0.0	13.3	26.7	26.7	13.3	13.3	13.3	13.3
10	0.0	0.0	0.0	0.0	0.0	0.0	0.0	0.0	0.0	0.0	0.0	0.0	0.0	0.0	13.3	26.7
	0.0	0.0	0.0	0.0	0.0	0.0	0.0	0.0	0.0	13.3	20.0	20.0	13.3	13.3	0.0	0.0

Table 6 The parameters k and c vs. inspection rate (%) of the contact lenses

c / k	0.5	1.0	1.5	2.0	2.5	3.0	3.5	4.0	4.5	5.0	5.5	6.0	6.5	7.0	7.5	8.0
1	0.0	0.0	0.0	0.0	64.0	100.0	100.0	100.0	100.0	100.0	100.0	100.0	100.0	100.0	100.0	100.0
	0.0	0.0	0.0	0.0	12.0	16.0	0.0	0.0	0.0	0.0	0.0	0.0	0.0	0.0	0.0	0.0
2	0.0	0.0	0.0	0.0	0.0	72.0	100.0	100.0	100.0	100.0	100.0	100.0	100.0	100.0	100.0	100.0
	0.0	0.0	0.0	0.0	16.0	20.0	12.0	0.0	0.0	0.0	0.0	0.0	0.0	0.0	0.0	0.0
3	0.0	0.0	0.0	0.0	0.0	0.0	56.0	88.0	100.0	100.0	100.0	100.0	100.0	100.0	100.0	100.0
	0.0	0.0	0.0	0.0	16.0	20.0	12.0	4.0	0.0	0.0	0.0	0.0	0.0	0.0	0.0	0.0
4	0.0	0.0	0.0	0.0	0.0	0.0	24.0	*92.0*	*100.0*	100.0	100.0	100.0	100.0	100.0	100.0	100.0
	0.0	0.0	0.0	0.0	24.0	40.0	72.0	*92.0*	*84.0*	72.0	16.0	0.0	0.0	0.0	0.0	0.0
5	0.0	0.0	0.0	0.0	0.0	0.0	0.0	20.0	76.0	100.0	100.0	100.0	100.0	100.0	100.0	100.0
	0.0	0.0	0.0	0.0	28.0	36.0	60.0	72.0	80.0	72.0	16.0	0.0	0.0	0.0	0.0	0.0
6	0.0	0.0	0.0	0.0	0.0	0.0	0.0	12.0	60.0	76.0	92.0	100.0	100.0	100.0	100.0	100.0
	0.0	0.0	0.0	0.0	8.0	20.0	52.0	64.0	72.0	72.0	0.0	0.0	0.0	0.0	0.0	0.0
7	0.0	0.0	0.0	0.0	0.0	0.0	0.0	0.0	44.0	72.0	84.0	100.0	100.0	100.0	100.0	100.0
	0.0	0.0	0.0	0.0	0.0	20.0	24.0	64.0	72.0	68.0	0.0	0.0	0.0	0.0	0.0	0.0
8	0.0	0.0	0.0	0.0	0.0	0.0	0.0	0.0	32.0	52.0	80.0	100.0	100.0	100.0	100.0	100.0
	0.0	0.0	0.0	0.0	0.0	0.0	24.0	64.0	68.0	48.0	0.0	0.0	0.0	0.0	0.0	0.0
9	0.0	0.0	0.0	0.0	0.0	0.0	0.0	0.0	20.0	52.0	80.0	96.0	100.0	100.0	100.0	100.0
	0.0	0.0	0.0	0.0	0.0	0.0	8.0	64.0	64.0	40.0	0.0	0.0	0.0	0.0	0.0	0.0
10	0.0	0.0	0.0	0.0	0.0	0.0	0.0	0.0	12.0	40.0	76.0	84.0	96.0	100.0	100.0	100.0
	0.0	0.0	0.0	0.0	0.0	.0	0.0	60.0	64.0	40.0	0.0	0.0	0.0	0.0	0.0	0.0

Table 7 The parameters effect on the inspection results of defect-free and defective samples

c / *k*	Large	Small
Large	A defect-free sample was correctly claimed as a nondefective one	A defect-free sample was claimed as a defective one, i.e., false alarm
	A defective sample would be claimed as a nondefective one, i.e., missed detection	A defective sample would be correctly claimed as a defective one. However, the "no-pass claim" should be regarded as spurious detection due to the fact that actual defects could not be exactly extracted in most case; only the remaining details were revealed
Small	A defect-free sample was correctly claimed as a nondefective one. However, the "pass claim" should be regarded as spurious correct result due to the fact that loose control limits can fortunately classify the redundant information as removable elements	A defect-free sample was claimed as a defective one, i.e., false alarm
	A defective sample would be claimed as a nondefective one, i.e., missed detection	A defective sample would be correctly claimed as a defective one. However, the "no-pass claim" should be regarded as spurious detection due to the fact that actual defects could not be exactly extracted in most case; only the redundant information was revealed

in illumination. Those two characteristics enhance the practicality of the scheme for industrial inspection. The shift invariance could be quite useful in the inspection of large object surfaces in real-world applications. In such a situation, single or multiple charge-coupled devices (CCDs) must capture a sequence of subimages under different fields of view. When the actuator is triggered to move the CCD to the next uncharted portion, the textures in each subimage will generally not be oriented in exactly the same manner and may be accompanied by slight shifting. The shift invariance characteristic of the proposed scheme will be useful for separately inspecting subimages of large objects more easily. In addition, illumination invariance makes the NMA suitable for illumination changes in the inspected image. This would reduce the false alarm or missed detection rate if the automatic optical inspection (AOI) system encounters unexpected light source instability in real-world applications, i.e., temporary underexposure or overexposure. Finally, experiments showed that the proposed scheme would be disturbed by image rotation because the trained basis space size is no longer suitable. In real-world applications, a precise fixture on the AOI hardware for object placement or an effective algorithm in the AOI software for image calibration would be a practical addition worth developing.

Acknowledgements This research is partially supported by the National Science Council, Taiwan, under contract no. NSC 97-2221-E-009-112-MY3. We would particularly like to thank Professor Andrew Yeh-Ching Nee, the associate editor, and the reviewers for constructive and helpful comments.

References

1. Kumar A (2008) Computer-vision-based fabric defect detection: a survey. IEEE Trans Ind Electron 55(1):348–363. doi:10.1109/TIE.1930.896476
2. Xie X (2008) A review of recent advances in surface defect detection using texture analysis techniques. Electron Lett Comput Vis Image Anal 7(3):1–22
3. Tsai DM, Hsieh CY (1999) Automated surface inspection for directional textures. Image Vis Comput 18:49–62. doi:10.1016/S0262-8856(99)00009-8
4. Perng DB, Chen SH, Chang YS (2009) A novel internal thread defect auto-inspection system. Int J Adv Manuf Technol. doi:10.1007/s00170-009-2211-8
5. Tsai DM, Chiang CH (2003) Automatic band selection for wavelet reconstruction in the application of defect detection. Image Vis Comput 21:413–431. doi:10.1016/S0262-8856(03)00003-9
6. Tsai DM, Wu SK (2000) Automated surface inspection using Gabor filters. Int J Adv Manuf Technol 16:474–482. doi:10.1007/s001700070055
7. Tsai DM, Lin CP (2002) Fast defect detection in textured surfaces using 1D Gabor filters. Int J Adv Manuf Technol 20:664–675. doi:10.1007/s001700200205
8. Guan SU, Xie P, Li H (2003) A golden-block-based self-refining scheme for repetitive patterned wafer inspections. Mach Vision Appl 13:314–321. doi:10.1007/s00138-002-0086-x
9. Lu CJ, Tsai DM (2005) Automatic defect inspection for LCDs using singular value decomposition. Int J Adv Manuf Technol 25:53–61. doi:10.1007/s00170-003-1832-6
10. Zontak M, Cohen I (2008) Defect detection in patterned wafers using anisotropic kernels. Mach Vision Appl. doi:10.1007/s00138-008-0146-y
11. Lu CJ, Tsai DM (2008) Independent component analysis-based defect detection in patterned liquid crystal display surfaces. Image Vis Comput 26:955–970. doi:10.1016/j.imavis.2007.10.007
12. Perng DB, Chen SH (2009) Automatic surface inspection for directional textures using principal component analysis. In: 20th Int Conf Prod Res
13. Paatero P, Tapper U (1994) Positive matrix factorization: a non-negative factor model with optimal utilization of error estimates of data values. Environmetrics 5:111–126
14. Lee DD, Seung HS (1999) Learning the parts of objects by non-negative matrix factorization. Nature 401(6755):788–791
15. Guillamet D, Vitrià J (2002) Non-negative matrix factorization for face recognition. Lect Notes Comput Sci 2504:336–344

16. Zhang D, Chen S, Zhou Z (2005) Non-negative matrix factorization for face recognition. Lect Notes Comput Sci 3723:350–363
17. Zaferiou S, Refas A, Buciu I, Pitas I (2006) Exploiting discriminant information in nonnegative matrix factorization with application to frontal face verification. IEEE Trans Neural Netw 17(3):683–695. doi:10.1109/TNN.2006.873291
18. Guillamet D, Schiele B, Vitrià J (2002) Analyzing non-negative matrix factorization for image classification. Int Conf Pattern Recognit 2:116–119
19. Liu W, Zheng N (2004) Non-negative matrix factorization based methods for object recognition. Pattern Recognit Lett 25(8):893–897. doi:10.1016/j.patrec.2004.02.002
20. Zhang J, Wei L, Miao Q, Wang Y (2004) Image fusion based on non-negative matrix factorization. Int Conf Image Process 2:973–976
21. Lee JS, Lee DD, Choi SC, Park KS, Lee DS (2002) Non-negative matrix factorization of dynamic images in nuclear medicine. IEEE Nucl Sci Symp Conf Rec 4:2027–2030
22. Ahn JH, Kim S, Oh JH, Choi S (2004) Multiple nonnegative-matrix factorization of dynamic PET images. In: Asian Conf Comput Vis 2004
23. Lee H, Cichocki A, Choi S (2006) Nonnegative matrix factorization for motor imagery EEG classification. Lect Notes Comput Sci 4132:250–259
24. Lee DD, Seung HS (2001) Algorithms for non-negative matrix factorization. Adv Neural Inf Process Syst 13:556–562
25. Lin CJ (2007) Projected gradient methods for nonnegative matrix factorization. Neural Comput 19(10):2756–2779
26. Lin CJ (2008) Matlab programs of alternating non-negative least squares with projected gradient. Available via DIALOG. http://www.csie.ntu.edu.tw/~cjlin/nmf/. Accessed 16 Feb 2009